

<https://doi.org/10.1038/s43246-024-00493-5>

Analyzing microstructure relationships in porous copper using a multi-method machine learning-based approach

Check for updates

Andi Wijaya , Julian Wagner, Bernhard Sartory & Roland Brunner

The prediction of material properties from a given microstructure and its reverse engineering displays an essential ingredient for accelerated material design. However, a comprehensive methodology to uncover the processing-structure-property relationship is still lacking. Herein, we develop a methodology capable of understanding this relationship for differently processed porous materials. We utilize a multi-method machine learning approach incorporating tomographic image data acquisition, segmentation, microstructure feature extraction, feature importance analysis and synthetic microstructure reconstruction. Enhanced segmentation with an accuracy of about 95% based on an efficient annotation technique provides the basis for accurate microstructure quantification, prediction and understanding of the correlation of the extracted microstructure features and electrical conductivity. We show that a diffusion probabilistic model superior to a generative adversarial network model, provides synthetic microstructure images including physical information in agreement with real data, an essential step to predicting properties of unseen conditions.

Machine learning algorithms have taken a big leap in the past few years¹. Their applications are far-reaching, e.g., for autonomous driving², natural language processing³, or speech recognition devices⁴. Recently data driven approaches have gained high interest, particularly to accelerate the material development from atomic scales to microstructure level^{5,6}. Consequently, machine learning (ML) has been used to identify the influence of chemical structures ranging from sub-angstrom-level to gross-level in relation to the property of interest¹. Deep learning has been used to predict material properties, e.g., ionic conductivity⁷, or mechanical properties^{8,9}.

Further, the recent development in deep learning provides exciting possibilities towards synthetic image generation¹⁰ enabling the possibility to predict material properties for unseen conditions, an essential ingredient for accelerated material design. Nevertheless, this has not been fully demonstrated so far. Deep generative models exhibit the ability to create complex structures^{11,12}. Various generative adversarial network (GAN)-based architectures have been developed in recent years targeting specific problems, e.g., X-ray image augmentation¹³, or molecular design¹¹. Although GAN shows high potential for microstructure prediction¹⁴⁻¹⁶, there are challenges concerning the stable training and mode collapse, causing serious problems when certain descriptors need to be extracted from the image data¹⁷. Notably, such an elicitation of physical descriptors or the microstructure features displays an essential requirement in material science.

Recently, denoising diffusion probabilistic models (DDPMs) for the generation of high-quality image synthesis have been introduced¹⁰. The model represents a parametrized Markov chain, which is trained utilizing variational interference to generate samples, matching the data after finite time¹⁰. Due to the recent development of this approach, up to now only view attempts in context to synthetic microstructure reconstruction have been performed in the field of material science¹⁸. It is important to point out, that for the prediction of material properties under unseen conditions, which represents an important asset towards accelerated material development, not only the synthetic image generation displays an important ingredient, but also the accurate extraction of the physical descriptors from the generated image data as well as correlation to the material property is essential. Hence, proper microstructure quantification as well as microstructure feature assessment is important to foster the understanding of the underlying processing-structure-property relationship. A methodology implying such considerations is still lacking.

The reliable extraction of microstructure features from a given microstructure depends on the experimental characterization method as well as on a time efficient and objective segmentation of the different material phases. Various approaches have been presented, e.g., for X-ray computed tomography (XCT)¹⁹ or for Scanning Electron Microscopy (SEM)²⁰⁻²². SEM-based methods provide advantages with respect to contrast

Materials Center Leoben Forschung GmbH, 8700 Leoben, Austria.

 e-mail: roland.brunner@mcl.at

and resolution. Nevertheless, fully automated segmentation of SEM image data especially for porous materials is challenging because of the ever-present shine through artifacts²³. Here, conventional segmentation methods are often limited due to misinterpretation of fore- and background information²⁴.

ML shows advantages to process complex and big microstructure data as well as to extract relevant morphological features obtained from SEM²⁵ or tomography-based methods²⁶. Recent studies show that deep learning algorithms are highly suitable for semantic image segmentation²⁷. In particular, the U-Net architecture²⁸ is considered as a highly valuable approach for most image segmentation workflows^{25,26,29}. However, further improvement of the prediction accuracy is mandatory for accelerated material design. Yet, the prediction accuracy not only relies on the model architecture but also concerns the efficiency of the annotation process. Usually the annotation of the present phases within the microstructure is performed manually³⁰. However, this is time-consuming especially for a large amount of data as well as heavily relies on user expertise. Hence, not appropriate for accelerated material design workflows. The need for rapid annotation for tomographic image data enabling an enhanced prediction accuracy beyond the state of the art is crucial rather than a supplement.

Further, the assessment of the relation between the microstructure features and the underlying material property is essential for accelerated material development. Multi-variable linear regression models convey an expressible relationship between two features or among several features³¹. For instance, those can be used to predict mechanical properties of alloys^{9,32,33} which are correlated with process parameters, alloy components, or microstructural features. SHapley Additive exPlanations (SHAP) analysis, originating from cooperative game theory can be utilized to measure the feature importance³⁴. Yet, a major difficulty for a proper assessment of the microstructure-property relationship often lies in the accuracy and statistical pertinence of the extracted microstructure features.

Herein, we develop a comprehensive methodology enabling proper microstructure quantification as well as the assessment of the microstructure feature dominance fostering the understanding of the underlying processing-structure-property relationship. Our findings highlight not only the importance of synthetic image generation and of accurately retrieving a set of microstructural features with statistical confidence for accelerated material design but also scrutinizing the features physical meaning in context to the material property. The presented methodology provides an essential step for the prediction of material properties, of unseen conditions, for porous materials.

As a representative porous system, we investigate different sintered porous copper materials. Such copper-based porous materials display a promising alternative to conventional interconnection technologies³⁵. We develop a multi-method machine learning-based approach incorporating tomographic focused image data acquisition, image segmentation, as well as microstructure feature extraction based on the segmented data, feature importance analysis and synthetic microstructure reconstruction. We collect three-dimensional (3D) image data by conducting ion beam-scanning electron microscopy (FIB-SEM). For an accurate microstructure feature evaluation, we develop a semantic image segmentation workflow based on a U-Net architecture incorporating an advanced annotation technique. Hence, an improved segmentation accuracy of about 95% is feasible. The extracted microstructural features are further used to perform a correlation analysis with different multi-variable linear regression (MVLRL) models to gain valuable clues about the relation of the microstructure features and electrical conductivity as well as associated sinter temperature. Here the best model, based on a defined set of microstructure features, attains an R^2 of 0.988. SHAP analysis is performed to assess the importance of the features on the electrical conductivity, a key for improved microstructure design. Ultimately, we perform synthetic image reconstruction for different sinter temperatures and electrical conductivities utilizing a conditional GAN model and a DDPM based on the preceding regression and feature importance analysis. The comparison identifies the DDPM as a highly

valuable model for microstructure reconstruction in material science. As a measure of the performance we utilize the physical descriptors or microstructure features extracted from the segmented synthetic and real images. The developed methodology is suitable to govern the electrical conductivity based on the underlying microstructure and vice versa. We point out, that the presented methodology and provided results are highly crucial to support the future design of complex porous structures in various fields.

Results

A need for an efficient annotation and deep learning microstructure segmentation

We conduct FIB-SEM tomography to image three different porous copper materials. For the first and second sample set, we use sinter pastes consisting of micro- and nanoparticles. Those sample sets are indicated as hybrid-paste material A (HPA) and B (HPB), respectively. The third sample set is composed of nanoparticles and is labeled as nano-paste material C (NPC), see Methods for further sample details. For the investigation of the microstructure evolution upon temperature, six sinter temperatures with 175 °C, 200 °C, 225 °C, 250 °C, 350 °C, and 400 °C are selected, see Fig. 1a. Each reconstructed 3D dataset comprises about 450 images with an image size of 1120×640 pixels² which makes an automated analysis approach indispensable, see Methods for further details regarding the image acquisition.

Here, we aim for an accurate classification of two phases, associated with the pore and copper, respectively, using a U-Net deep learning architecture from Chollet³⁶ (see Supplementary Note 1 and 2). For an accurate prediction, the need of an efficient training for the U-Net model is apparent^{25,37}. Figure 1b shows a representative cross section obtained from the SEM-FIB tomography data. Here, the segmentation of the so-called shine through artifact³⁸ within the pore is challenging. Infiltration of the pore³⁸ might work but would extend the expenditure. In the following we compare various segmentation approaches. As shown in Fig. 1b, a conventional threshold algorithm (CTA)³⁹ segmentation, as shown as yellow overlay, is not able to deal with all shine through artifacts within the pore phase. The CTA assigns the pore phase correctly with darker gray values but fails for regions with similar gray values to the copper phase. Therefore, we conduct a hybrid approach to provide a more accurate training for the U-net model. For this semi-automatic hybrid approach³⁵, a two-step procedure is used. First, the selection of a threshold between the pore and copper in the second derivative histogram plot is selected, see Fig. 1c. Figure 1d illustrates with a color map the associated pore and copper phases, based on the selected threshold at the first peak of the second derivative histogram. Within the second step we conduct the simple linear iterative clustering (SLIC) algorithm for superpixel generation⁴⁰, see Fig. 1e. Each superpixel segment's average gray value is calculated and is segmented with the threshold obtained in the first step. Figure 1f depicts the segmented pore phase utilizing the introduced hybrid method. The segmentation includes also the non-detected shine through artifacts. Figure 1g illustrates the annotation for the U-net model, see Supplementary Note 1 and 2 for further details. We are able to annotate, based on the results from the hybrid segmentation, 0 for copper, 1 for the pore detected by the conventional threshold, and 2 for the shine-through artifacts. More details with respect to the training are provided in the Methods section. Figure 1h, i shows the output for the pores in 2D and both pores as well as copper in 3D, respectively utilizing the U-Net segmentation trained with the hybrid model.

We validate the segmentation performance using known metrics⁴¹ such as Jaccard Index, precision, recall, and accuracy, see Table 1. A manually segmented dataset with the support of the Avizo software is used as the ground truth. Further details are presented in Supplementary Note 3. Overall, the U-Net using the hybrid annotation workflow provides the best performance. Our work shows that a U-Net architecture with semi-automatic annotation, is capable to provide segmentation with an accuracy of up to 94%, which is higher than previously reported with U-net architectures⁴².

Three-dimensional copper network formation upon sintering

For an improved design of the microstructure in context to the targeted property, it is essential to understand the correlation between the physical descriptors describing the microstructure and the property. Figure 2a

illustrates the segmented 3D microstructure for sample HPA, HPB and NPC, utilizing the U-net model based on the semi-automatic hybrid annotation. Here, exemplary the segmented volume of interest (VOI) for 175 °C is shown. The microstructure exhibits significant differences for the

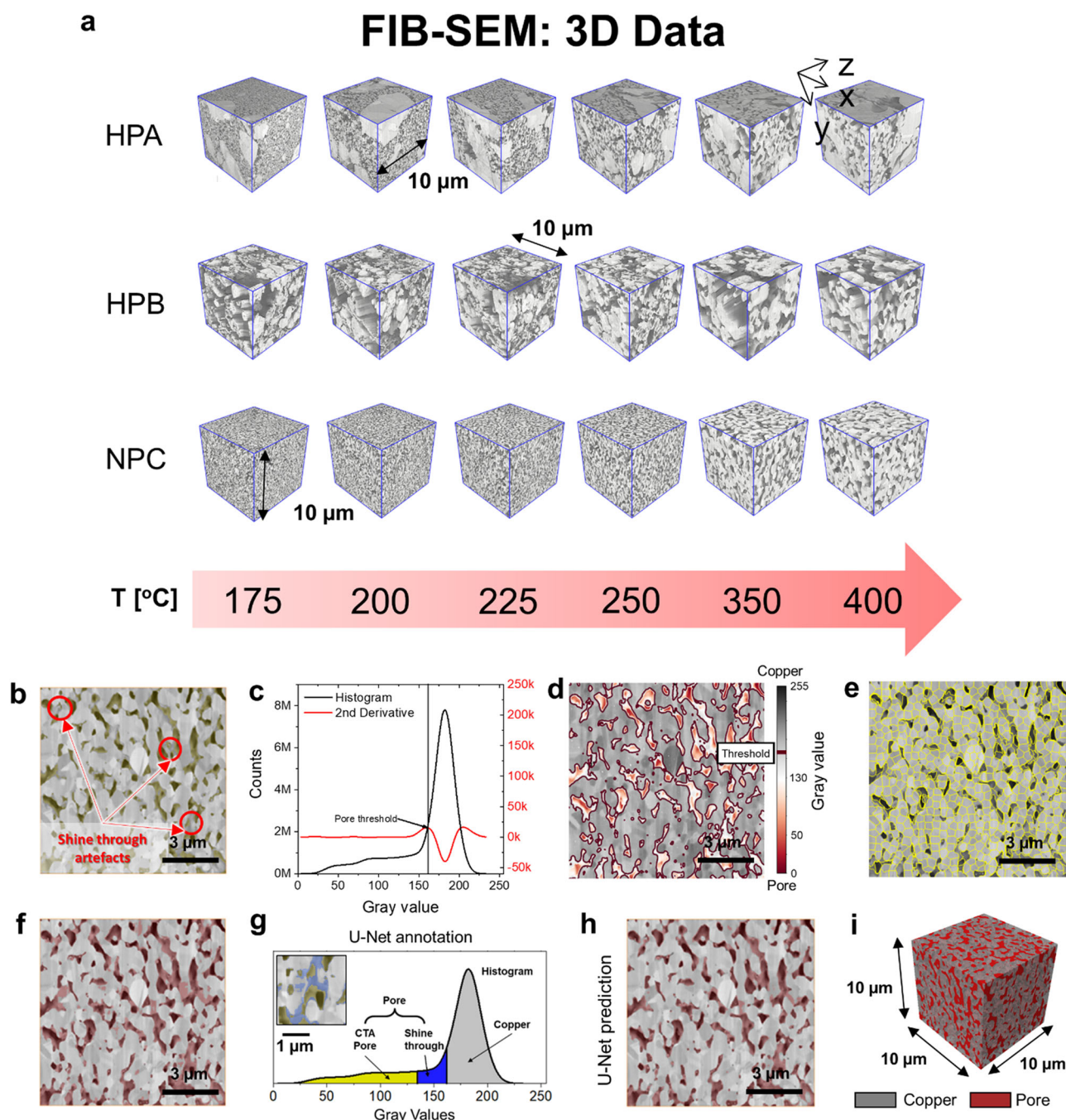


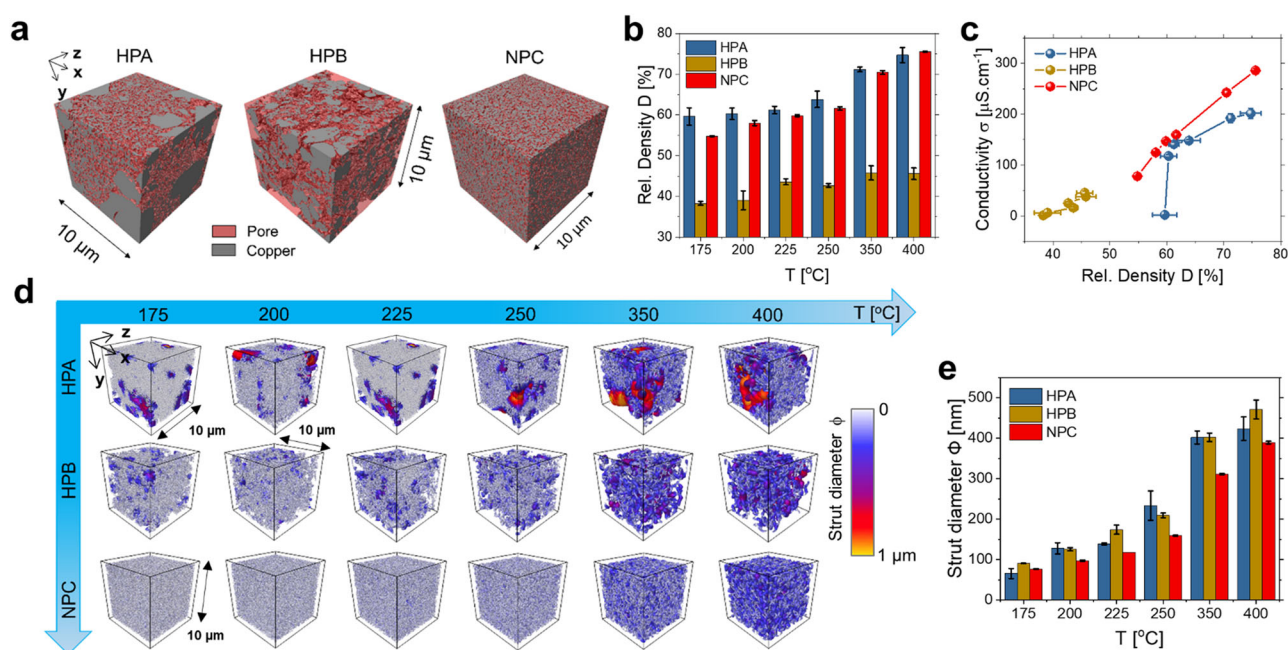
Fig. 1 | Segmentation challenges, annotation for the U-Net model and associated results. **a** 3D morphology representations of the three different copper configurations (HPA, HPB, and NPC) for different sinter temperatures. HPA and HPB exhibits a microstructure which consists of micro- and nanosized pores. NPC exhibits a microstructure with nanosized pores for all temperatures. **b** Challenging are the shine-through artifacts within the SEM image. As illustrated conventional threshold algorithms (CTA) usually segment the pores (yellow) incomplete. **c** The second derivative of the histogram is performed to pre-select the threshold between the pore and copper phase for the hybrid image analysis approach. **d** Gray value range is illustrated by a color map from red to gray, projected on the SEM image. Threshold between the copper and pore phases is depicted from the second derivative histogram, as indicated in the image. **e** Simple linear iterative clustering (SLIC)

for superpixel generation is utilized. Accuracy of the segmentation is increased by utilizing the superpixel's average grayscale threshold, obtained from the second derivative method. **f** The hybrid segmentation shows an efficient and fast method to segment the pore and copper phase. **g** Improved segmentation accuracy can be achieved by the introduced annotation method for the U-Net model. Three phases are depicted in the histogram associated with the copper, pore, and shine-through artifact domains associated with the labels 0 (gray), 1 (yellow) and 2 (blue), respectively based on the hybrid segmentation, see inset. The pore volume is given by pores detected with the CTA (yellow) and the shine-through artifacts (blue). **h** U-Net model trained with the hybrid segmentation approach illustrating the segmented pores (red). **i** 3D representation illustrating the segmented copper (gray) and pores (red), reaching an accuracy of 94%.

Table 1 | Segmentation quality

Segmentation method	Jaccard Index		Precision		Recall		Accuracy
	Pore	Copper	Pore	Copper	Pore	Copper	
CTA	0.69	0.81	0.98	0.81	0.70	0.99	0.87
Hybrid	0.77	0.82	0.83	0.93	0.92	0.88	0.89
U-Net CTA	0.59	0.77	0.98	0.77	0.60	0.99	0.83
U-Net Hybrid	0.86	0.89	0.89	0.96	0.96	0.92	0.94

We compare several metrics, e.g., Jaccard Index, precision, recall, and accuracy to validate the segmentation results for the pore and copper. For the segmentation, we use the CTA, the hybrid algorithm as well as the U-Net predictions trained by the CTA and the hybrid algorithm.

**Fig. 2 | Segmented Volume of interest, relative density and copper strut size.**

a Segmented volume of interests (VOIs) with $10 \times 10 \times 10 \mu\text{m}^3$ for sample HPA, HPB and NPC, exemplary for 175 °C, with the copper (gray) and pore (red) phases. Scale bar is 10 μm . **b** Evaluated relative density D as a function of the sinter temperature for HPA (blue), HPB (gold) and NPC (red) extracted from the segmented VOIs. **c** Electrical conductivity σ vs. relative density D for HPA (blue), HPB (gold) and NPC (red). **d** Skeletonized copper phases illustrate the 3D copper struts

distributions for sample HPA, HPB and NPC between 175 °C and 400 °C. Each VOI is $10 \times 10 \times 10 \mu\text{m}^3$. Color coding indicates the strut diameters variation within the volume ranging from 0 (white) to 1 μm (yellow). **e** Statistical analysis of the strut diameter ϕ for different temperatures and sample sets. Sample HPA, HPB and NPC are indicated by blue, gold, and red, respectively. All the quantification plots in this work show the means and the 95% confidence intervals except those stated otherwise.

three materials HPA, HPB and NPC. NPC indicates a nano-porous network with a porosity of 45.2% at 175 °C. HPA and HPB show micron-sized as well as nano-sized pores within the VOI, however, they differ in the porosity with 42.4% and 61.7% at 175 °C, respectively. Figure 2b shows the densification^{43,44} of the three porous copper configurations upon sintering. Here, the relative density D is defined as the ratio of the copper volume to the total volume of the VOI. The hybrid-paste HPA and nano-paste NPC exhibits, compared to HPB, a rather similar behavior for the densification. The changes in the relative density from 175 °C to 400 °C for HPA and NPC material are about 18.5% and 20.8%, respectively. The hybrid-paste HPB shows the highest porosity and depicts a different behavior upon sintering. Here, the densification gives about 7.3%.

We inverse the specific resistivity obtained from the 4-point probe measurement to obtain the electrical conductivity σ . The superior electrical performance of the nano-paste is demonstrated in Fig. 2c. Although the relative densities D for HPA and NPC are similar, there are significant differences of $50.2 \mu\text{S.cm}^{-1}$ and $84.3 \mu\text{S.cm}^{-1}$ in the electrical characteristics of σ_{NPC} and σ_{HPA} at 350 °C and 400 °C, respectively.

For the evaluation of the copper strut diameter ϕ and its evolution upon sintering, we skeletonize and statistically analyze the segmented data²⁴

(Fig. 2d, e). The mean values are obtained by fitting the log-normal distribution of the strut diameter histograms (Supplementary Note 4). We observe an increase of ϕ with temperature. This behavior is linked to the continuous growth of the bonds between the sinter particles due to the increase in temperature⁴⁵. The NPC material indicates a small variation of the copper strut diameter. The 95% confidence interval lies within a range of 0.01–3.5 nm and suggests a highly homogenous distribution of the copper network as indicated for the volumetric microstructure data in Fig. 2d. For HPA and HPB, the confidence interval lies within 2.4–36.4 nm and 0.7–23.6 nm, respectively, and is significantly larger than for the NPC material.

Evolution of the copper strut-interconnectivity and investigation on the surface properties upon cycling

Another significant microstructural feature concerns the connectivity of the copper strut and its evolution upon sintering, see Methods. We use the geodesic tortuosity τ^{46} as a measure for the strut interconnectivity. A high tortuosity of the copper relates to a small copper strut interconnectivity. The geodesic tortuosity is defined by the ratio of the geodesic distance to the Euclidian distance. Figure 3a illustrates the evaluated 3D tortuosity along the

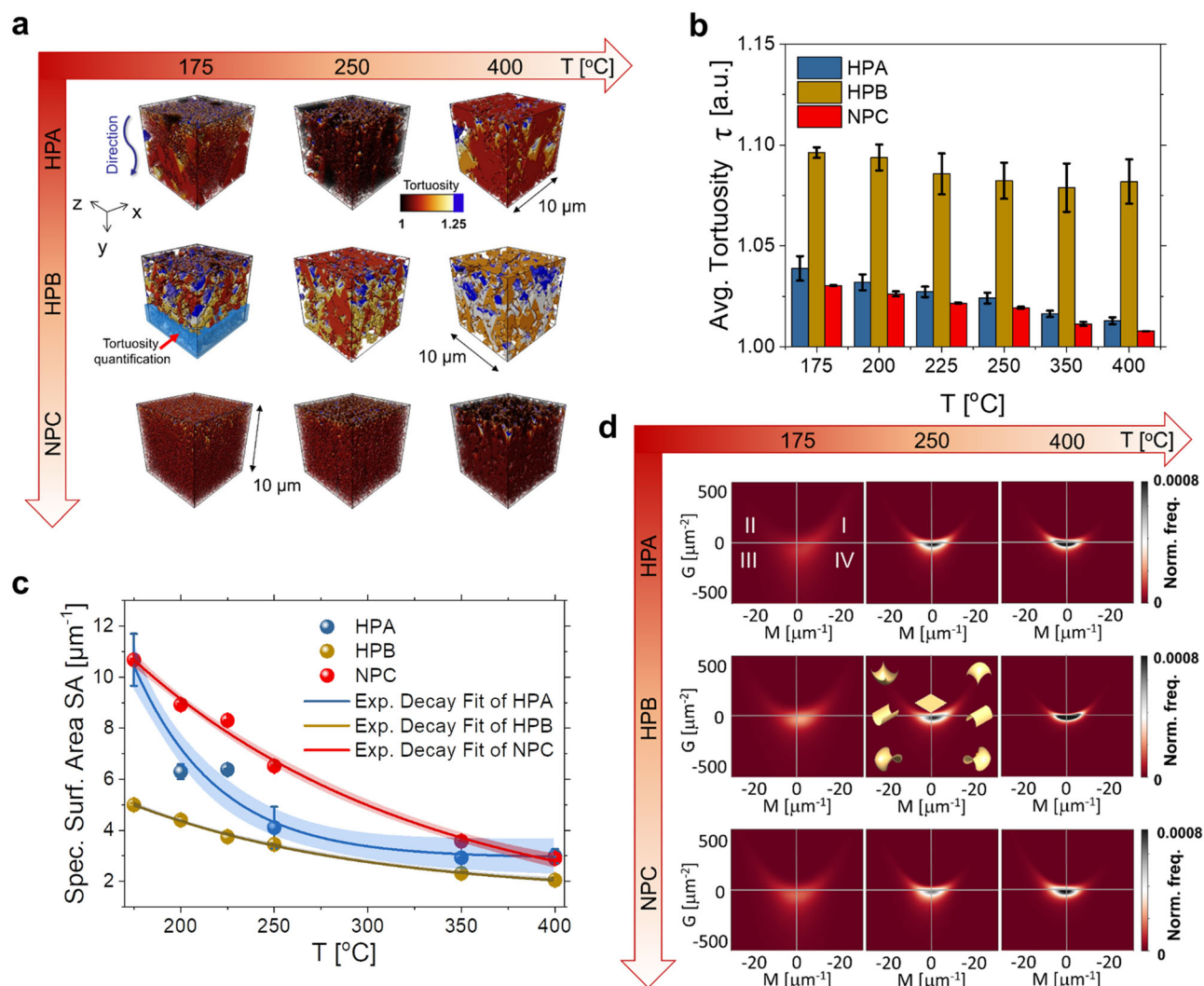


Fig. 3 | Strut interconnectivity, surface and copper-pore interface analysis upon sintering. **a** 3D tortuosity analysis in the y direction to quantify the connectivity of the copper along the direction from the surface to the substrate, with high tortuosity (blue) and low tortuosity (black). **b** Evolution of the averaged tortuosity upon sintering for HPA (blue), HPB (gold) and NPC (red). For the analysis we average the values of the last 25% of the volume, as highlighted for the 3D volume for HPB at 175 °C in five directions (see Supplementary Note 5). **c** Specific surface area analysis for HPA (blue), HPB (gold) and NPC (red), respectively. All samples indicate a reduction of the specific surface area. **d** The complexity of the sintering process is illustrated by joint distributions of the Gaussian (G) and mean (M) curvatures. All

materials' tails stretch in the first quadrant (QI) and second quadrant (QII). The QI tails show the presence of small radii convex regions, inversely related to the magnitudes. Consequently, the low temperature plots show the early stage of sintering. In contrast, the QII tails show the progress of sintering when the particles are joining. This progress indicates the formation of necks and concave radii. Interestingly as temperature increases, the QI tails tend to get shorter and the QII tails tend to get denser and longer. The intensity maximums/peaks show negative Gs for all samples at low temperatures. As the temperature increases, the necks become flattened, i.e., G becomes less negative.

y-direction, which conforms to the direction from the surface to the substrate, exemplary for 175 °C, 250 °C and 400 °C. The tortuosity τ is quantified by averaging the extracted tortuosity values along the y-direction of the last 25% from the sample's length³⁸. Further information with respect to the tortuosity is provided in Supplementary Note 5 where we calculate the overall tortuosity in five directions and average them.

As indicated by the 3D tortuosity distribution in Fig. 3a and the calculated averaged tortuosity in Fig. 3b, the HPB material indicates the highest tortuosity of the copper strut in comparison to HPA and NPC. As shown in Fig. 3b, for HPA and NPC the average tortuosity decreases between 175 °C to 400 °C from 1.039 to 1.013 and from 1.030 to 1.008, respectively. The NPC material, as indicated in Fig. 3a, illustrates the lowest tortuosity distribution within the analyzed VOIs for all temperatures.

During the sintering, the surface area is reduced by the growing of bonds between the sinter particles. The driving force for the sintering decreases as the surface area is annihilated. The decline of the specific surface

area SA with the sinter temperature is shown in Fig. 3c. At 175 °C, the specific surface area for HPA and NPC is about a factor of two larger than for HPB. SA_{HPA} decays very fast from 175 °C to 200 °C. Consequently, it starts to decay slowly after 200 °C. SA_{HPB} and SA_{NPC} decays in a more constant manner with temperature. The sample HPA and NPC reaches a similar SA at 400 °C. The value for HPB is about 30% smaller.

Further, we investigate the pore-copper interface evolution upon sintering using the Gaussian curvature G and mean curvature M⁴⁷. Both curvatures classify the local surface geometries with their joint distributions⁴⁸. Figure 3d depicts the G-M curvature joint distributions of the copper surfaces for different sinter stages. In the first (QI) and second (QII) quadrants, two tails extend to high mean curvature values. The changes of those tails with temperature indicate the change of the copper particles' convexity. The copper particles' local geometries at the lower sinter temperature, display mostly cup-convex surfaces resembling spheroidal structures⁴⁹, therefore, their Ms are positive. The sintering process reduces the sphericity of the

Table 2 | MVLR models: RMSE and R² from LOOCV and test sets

Notation:					
<i>D</i>	Relative density				
<i>SA</i>	Specific surface area				
ϕ	Strut diameter				
τ	Average tortuosity				
<i>G</i>	Gaussian curvature				
<i>M</i>	Mean curvature				
α	Bruggeman exponent				
β	$M / (G \cdot \phi)$				
Model	Features	Training	Testing		
		LOOCV RMSE	R ²	RMSE	R ²
A	τ, G	21.8	0.956	35.1	0.707
C	SA, τ, G	22.1	0.956	35.2	0.707
I	SA, ϕ, τ, G	22.7	0.960	36.5	0.684
J	SA, α	13.1	0.982	25.1	0.851
N	SA, G, α	13.4	0.983	25.0	0.852
Q	SA, α, β	11.5	0.988	21.9	0.887
R	SA, M, ϕ, α	14.0	0.985	23.3	0.871

Different models are presented including information about the features used. The models A, C, and I are linear between 10 to 200 $\mu\text{S}\cdot\text{cm}^{-1}$. For the models J, N, R and Q additional engineered features (α β) are applied. For the latter models a linearity between 0 to 285 $\mu\text{S}\cdot\text{cm}^{-1}$ is achieved.

particles. As a result, the emerging tails in QI are getting less pronounced by increasing the temperature for all presented materials. The observed behavior is complemented with an increased number of cup-concave geometries indicated by more pronounced tails in QII.

The intensity maximum close to the origin of the graph shows negative *G*s for all samples. For HPB the magnitude of *G* is decreasing which suggests an increase of the neck's radii during sintering. The sinter process also causes a reduction of the particles' convexity leading to a decrease of the mean curvature for the higher porosity material HPB (Fig. 3d). Supplementary Note 6 provides the *G* and *M* at each sinter temperature. At 175 °C for the material HPA, G_{HPA} is $-146 \mu\text{m}^{-2}$. Its negative value indicates that necks with small radii saddle-like surfaces are prevalent. The positive M_{HPA} of $2.18 \mu\text{m}^{-1}$ shows that the incidence of convex structures is quite dominant. Therefore, spherical geometries of HPA's nanoparticles are still abundant. This type of surface illustrates that HPA is still in an early stage of sintering⁵⁰; therefore, the particles are just starting to coalesce and their necks are newly formed. As the temperature is increased, the particles are coarsened. As a result, the necks radii are flattened and its *G* magnitude is decreased towards zero. Subsequently, the small radii nanoparticles' convex surfaces are diminishing and *M* decreases. This trend continues and G_{HPA} and M_{HPA} reaches $-16 \mu\text{m}^{-2}$ and $-1.72 \mu\text{m}^{-1}$ at 400 °C, respectively.

G_{NPC} and M_{NPC} at 175 °C is $-102 \mu\text{m}^{-2}$ and $-0.93 \mu\text{m}^{-1}$, respectively. NPC shows a more positive *G* than for HPA. Therefore, the necks radii are larger than for HPA. The negative value of M_{NPC} indicates the reduction of convex surfaces for the nanoparticles. Here, the material is in a more advanced stage than HPA at this temperature. Indeed, the electrical conductivity σ_{HPA} and σ_{NPC} at 175 °C is 2.3 $\mu\text{S}\cdot\text{cm}^{-1}$ and 78.2 $\mu\text{S}\cdot\text{cm}^{-1}$, respectively. This finding is in line with the tortuosity analysis and it provides further insight into the enhanced electrical property of the material NPC.

Microstructure feature importance and mathematical relationship of microstructural features and electrical behavior

The evaluation of the microstructure features, their physical analysis, as well as their correlation to the material property display crucial ingredients for accelerated material design. In the previous sections, we qualitatively tried to explain the correlation between the extracted microstructure features and the electrical behavior of the material. The understanding of such

correlations, however, is challenging due the underlying complexity and multi-faceted problems. Here, we establish a mathematical relationship between the microstructure and property by applying a machine learning-based deployment in the form of a linear regression model^{1,51}, see Methods.

We build various multi-variable linear regression (MVLR) models that shall enable us to provide the microstructure features or independent variables as an input and the targeted electrical conductivity or dependent variable as a predicted output. As a result, the structure-property relationship can be defined arithmetically. We train the models with at least two microstructure features obtained from the segmented VOIs. The coefficient's sign of each feature is used to indicate the dependence of the feature with respect to the electrical conductivity, see Supplementary Table 1. We use a leave-one-out cross-validation (LOOCV) to obtain reliable and unbiased results⁵² for the training, see Methods. We test different MVLR models based on different microstructural feature combinations, see Supplementary Table 2. For the prediction of the electrical conductivity, we define three different microstructure sets, as an input for the MVLR, which are not used as training data sets, see Supplementary Note 8. Subsequently, the outcomes are compared with the experimental data.

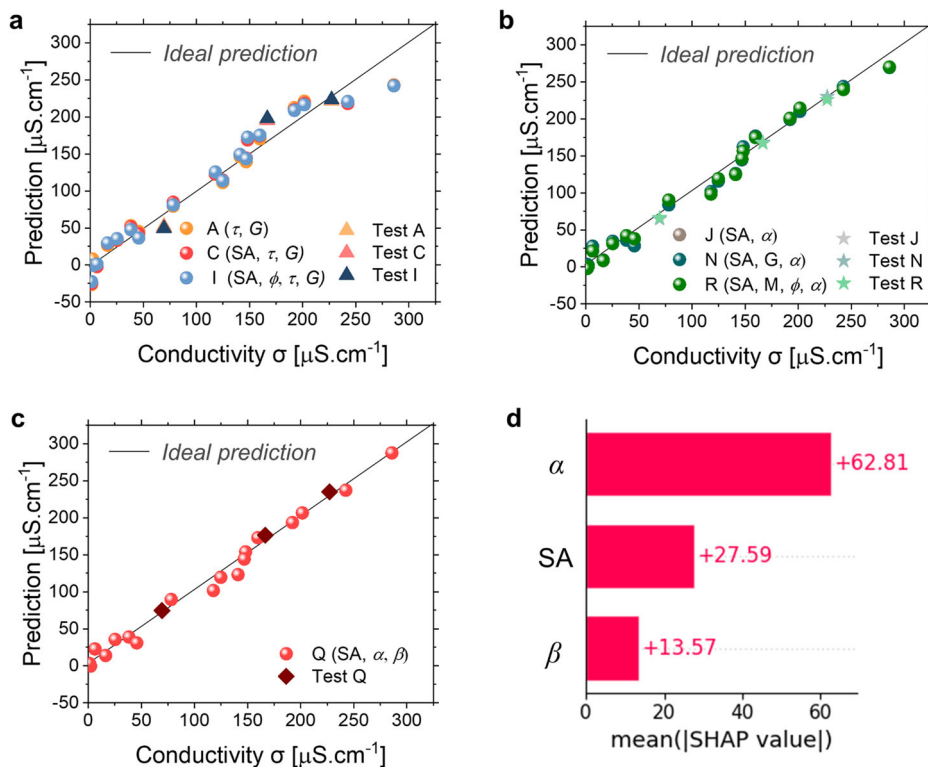
The various MVLR-based models are summarized in Table 2. Figure 4a illustrates the regression analysis for the models A, C and I. The models labeled as A, C, and I incorporate different raw features, like the relative density, specific surface area, strut diameter, average tortuosity, and Gaussian and mean curvatures. Model A, C and I provide R² values of 0.956, 0.956, and 0.960, respectively. Here, the linearity lies within the range of about 10–200 $\mu\text{S}\cdot\text{cm}^{-1}$. Outside of this conductivity range, predictions are inaccurate. In order to enhance the prediction, we perform feature engineering to boost the model performance with mathematical transformation⁶. Therefore, we augment two additional features, labeled with α and β , taking mathematical correlations between different features into account. α incorporates the correlation between the relative density *D* and the tortuosity τ according to the Bruggeman equation⁵³ with $\tau = D^{-\alpha}$. The second feature is defined by $\beta = M / (|G| \cdot \phi)$. Further details are provided in Supplementary Note 7. The corresponding models utilizing the additional features are labeled with J, N, R and Q. The results are displayed in Fig. 4b and Fig. 4c respectively.

Indeed, as illustrated in Fig. 4b and c the utilization of the additional features improve the linearity from 0 to 285 $\mu\text{S}\cdot\text{cm}^{-1}$. In particular, the MVLR-based model Q provides the best performance, as indicated by Table 2. Further, we assess the importance of the features for the model Q utilizing a SHapley Additive exPlanations (SHAP) analysis³⁴. The global impact of the features is calculated with the mean of the absolute SHAP values. Figure 4d illustrates the impact of each feature from the highest to the lowest. The analysis indicates that the feature α , which relates to the tortuosity and relative density by the Bruggeman equation, provides the highest impact on the electrical conductivity, followed by the specific surface area *SA*, and β . The results provide guidelines for the microstructure design, uncovering the most critical microstructural features for the electrical conductivity.

Synthetic image reconstruction of the porous microstructures for different sinter temperatures and electrical conductivity values

A promising approach to reconstruct the microstructure for a given material parameter is by utilizing deep generative models^{14,54,55}. In particular, we apply a denoising diffusion probabilistic model (DDPM) architecture. A DDPM is a parameterized Markov chain and consists of forward and reverse diffusion processes¹⁰. The forward process adds different Gaussian noise levels to the images, and the reverse process denoises the images with a neural network to find the added noise distribution to each training data. Original microstructure images can be reconstructed by removing the noise⁵⁶. By applying the trained model to an image sampled from pure noise, the model can denoise it to generate images similar to the real dataset⁵⁶, see Fig. 5 and the Methods section for further details in context to the DDPM. In addition, we compare the results obtained from the DDPM with a

Fig. 4 | Regression and microstructure feature importance analysis in context to the electrical conductivity. **a** Prediction results for MVLR model A, C and I versus the measured electrical conductivity. Only raw features are used. Here a linearity is provided from 10 to 200 $\mu\text{S}\cdot\text{cm}^{-1}$, which is not for the whole experimental window. We validate the models' performance with three test sets, indicated by Test A, C and I, not used for the training, to find the best model. **b** Improved prediction results for model J, N and R incorporating the engineered feature α in combination with raw features. The performance of the model is validated with three test sets indicated by Test J, N and R. **c** Prediction result for Model Q with the raw feature SA, and the engineered features α and β . Model Q shows the best performance with an improved linearity across the experimental window of 0 to 285 $\mu\text{S}\cdot\text{cm}^{-1}$. The model performance is validated with the test set indicated by Test Q. **d** The importance of the feature is assessed by SHAP. The analysis indicates that α represents the most important feature for the electrical conductivity, followed by SA and β .



conditional generative adversarial network (cGAN). The generator within the cGAN architecture generates synthetic images at each training cycle based on the provided input. The discriminator determines the authenticity of the reconstruction. As the training progresses, synthetic images are produced by the generator, see Fig. 5 and Methods section.

Figure 5a, d, g show the segmented real microstructure indicated by the pore and copper phases for different sinter temperatures. For the segmentation the introduced U-Net architecture, trained with the hybrid model, is used. In addition, in Fig. 5b, e, h and Fig. 5c, f, i the reconstructed synthetic microstructure images depicted from the cGAN model and DDPM, respectively, are illustrated. Clearly the change of the microstructure with temperature is represented for both models. A quantitative performance analysis is important to assess the prediction result in more detail.

Evaluation of the model performance

The next step is to assess the quality of the reconstructed synthetic images. As illustrated here¹⁶, Fréchet inception distance (FID) as well as precision and recall are not suitable to measure the quality of synthetic microstructure data. Here, we assess the quality of the synthetic images based on extracted physical descriptors of the microstructure or microstructural features⁵⁷.

In particular we validate the model performance by comparing the evaluated relative density, specific perimeter, as well as shape index for the real and synthetic microstructures in relationship to the sinter temperature, see Fig. 6. The critical descriptors are also related to the electrical conductivity. Further, we extract the R^2 for the three descriptors individually, as well as the average of R^2 for all three physical descriptors, see Table 3. The presented assessment of the synthetic microstructures in Fig. 6 and Table 3 illustrate the superiority of the DDPM over the cGAN model. The largest deviation between the two models is observed for HPA and HPB. Both exhibit a more inhomogeneous microstructure than NPC, which makes the prediction with the GAN more challenging. Nevertheless, as illustrated in Fig. 6 and Table 3 even for the NPC material, which illustrates a homogeneous nano-porous structure, the DDPM predicts better than the cGAN.

Discussion

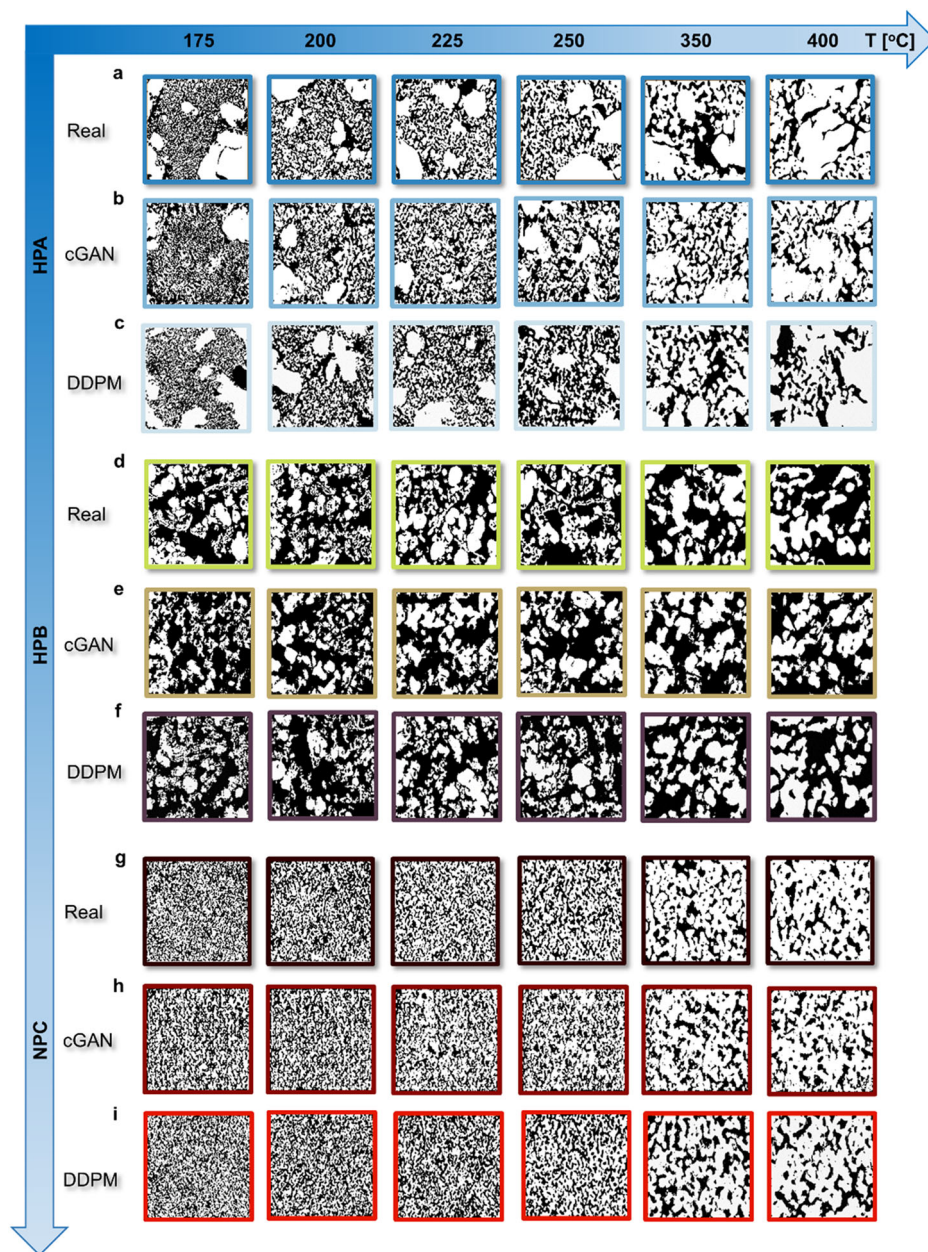
Due to the complexity of the process-structure-property relationship for porous materials, a single mathematical formulation from the porosity and the material parameter dependence⁵⁸ is not sufficient. The microstructure can be quantified by the physical descriptor or microstructure features. However, not every microstructure feature impacts the underlying material property equally. Detailed knowledge about the interplay of the feature with the property generates guidelines for the design of the microstructure within the processing step. Our work shows that the electrical conductivity is clearly more affected by the alteration of certain microstructural features. Therefore, to generate accurate guidelines it is highly important to retrieve the microstructural features accurately with adequate statistical confidence as well as to understand their physical meaning in context to the processing and material properties.

Further, the presented methodology enables us to gain an understanding about the correlation between the microstructure and the electrical conductivity utilizing a multi-variable linear regression (MVLR) model. The microstructural features, which are obtained from the microstructure analysis, change non-monotonically which makes the prediction of the electrical conductivity based on the microstructure complicated. Usually, MVLR models working with categorical variables, i.e., each material is assigned to a numerical value⁵⁹, provide a non-satisfying deployment for an accelerated material design. Such approaches need prior knowledge about the material category and a general expression, which usually cannot be attained easily. However, the presented MVLR model is suitable for the generalization of the conductivity prediction from microstructural features.

Hence, the presented MVLR model can produce a highly linearized correlation with an R^2 of 0.986 for model Q. The substantial perception of the microstructural features and their correlation is crucial for the model's performance as well as to deliver microstructure design guidelines for the production. Indeed, as depicted from the SHAP global impact analysis, α represents a highly dominating factor among the other features to determine the conductivity of model Q.

The MVLR model provides information about the interplay but is not suitable to predict the microstructure with high accuracy. It may rather

Fig. 5 | Synthetic microstructure reconstruction utilizing a conditional generative cGAN model and DDPM. **a, d** and **g** illustrate the segmented microstructures for the porous materials HPA, HPB, and NPC obtained with FIB-SEM. **b, e** and **h** correspond to the predicted (synthetic) microstructures utilizing the cGAN model for HPA, HPB, and NPC, respectively. **c, f** and **i** correspond to the predicted (synthetic) microstructures utilizing the DDPM for HPA, HPB, and NPC, respectively. The synthetic and experimentally retrieved (real) microstructures are plotted for different sinter temperatures. The segmented copper and pore phases are illustrated in white and black, respectively. The frame colors are related to the porous materials (HPA, HPB and NPC), real and predicted microstructures.



provide an estimate about the spatial extent in context to the microstructural feature space. For the definite reconstruction of the microstructure, we utilize a conditional GAN (cGAN) model and diffusion-based model (DDPM). The work highlights how a cGAN and DDPM architecture renders possibilities for the reconstruction of synthetic microstructure images. The presented work indicates that the microstructure can be reconstructed synthetically for an allocated conductivity with significant quality, especially utilizing the DDPM. Clearly for the synthetic generation of the materials microstructure it is shown that the DDPM is superior to the cGAN model. The inferiority of cGAN might originate from its architecture prone to unstable training and mode collapse¹⁷. Such generated reconstructed synthetic images can be further utilized for morphological analysis^{16,60,61}.

Indeed, the developed unique workflow paves the way towards machine learning driven accelerated material design. The findings in this paper are not only limited to the conductivity prediction of sintered porous materials but also suggest broader applications to other porous microstructures and material properties. Ultimately, we point out that the provided results illustrate the potential of machine learning to support the design of complex structures for advanced material manufacturing, e.g., of

solid oxide electrolysis cell^{62,63}, solid state materials for batteries⁶⁴, power semiconductors⁶⁵, batteries^{26,29,66}, electro ceramics⁶⁷ or hydrogen storage⁶⁸ as well as provides an essential step to predict properties of unseen conditions.

Methods

Porous copper preparation

Three copper pastes have been developed by Dycotec Materials Ltd and Intrinsic Materials. They consist of micro- and nanoscale size copper, solvents, organic metal precursors, and organic binders. The size of nanoparticles and microparticles is about 150 nm and approximately within a micrometer, respectively. Two other differences are the viscosity and solid content of the copper pastes. At ambient conditions and with a shear rate of 50/s, leading to different viscosities of HPA, HPB, and NPC. In addition, the solid content of HPA, HPB, and NPC are 78.8%, 76.0%, and 84%, respectively. The pastes are stencil printed on 200 mm wafers. The samples are dried immediately in a YES-PB8 high pressure vacuum furnace (Yield Engineering System) to evaporate the solvent and to solidify the paste. Both pre-curing and curing are done with a SRO700 single-wafer furnace (ATV Technologie GmbH).

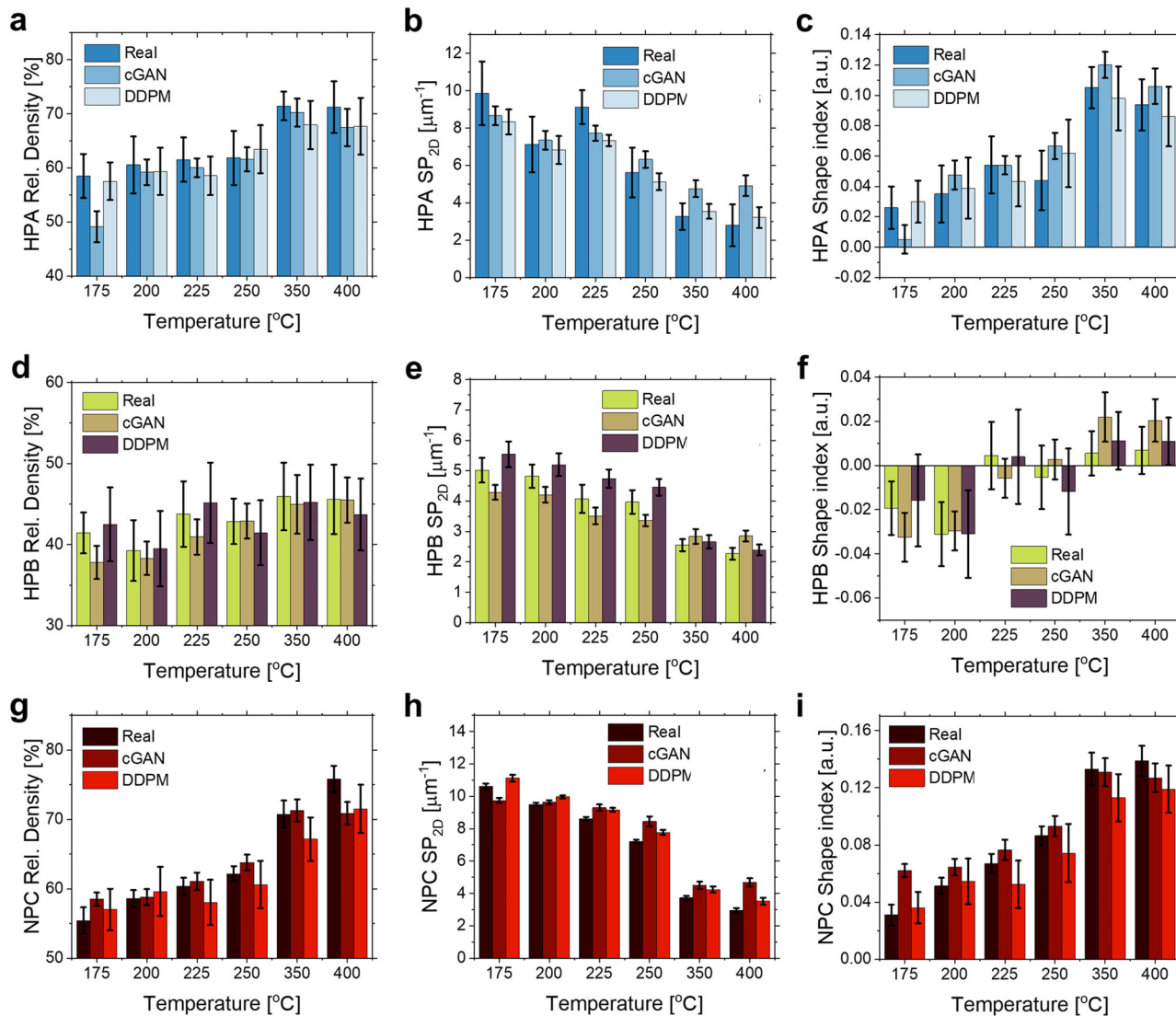


Fig. 6 | Image quality assessment for the cGAN model and DDPM based on the extracted microstructure features. Evaluated relative density, specific perimeter (SP_{2D}), and shape index for the segmented real microstructures, and the synthetic microstructures for the cGAN model as well as for the DDPM (from left to

right): (a–c) for HPA, (d–f) for HPB, and (g–i) for NPC. The legend in the graph indicates the associated colors for the real microstructures as well as for the predictions performed with the cGAN model and DDPM. For all plots the standard deviation is indicated.

4-point probe measurements

The SRO700 furnace is installed with an in-situ four-point probe by T.I.P.S. Messtechnik GmbH. This is used to monitor the electrical resistance of the copper pastes during sintering process. First, the probe's four equidistant copper tips are brought into contact with the surface. Second, the tips are

connected to a multimeter and a voltmeter. Then, 1 A current is directed through the two outer probes and the voltage is measured between the inner two probes.

Table 3 | Evaluated R^2 to assess the synthetic image quality

Sample	R^2		Relative density D		Specific perimeter SP_{2D}		Shape index		Avg. of physical descriptors	
	cGAN	DDPM	cGAN	DDPM	cGAN	DDPM	cGAN	DDPM	cGAN	DDPM
HPA	0.33	0.76	0.75	0.86	0.72	0.89	0.60	0.84		
HPB	0.28	0.72	0.69	0.83	0.34	0.92	0.44	0.82		
NPC	0.88	0.86	0.87	0.97	0.34	0.92	0.87	0.90		

Comparison of the different R^2 values for the relative density D , the specific perimeter SP_{2D} , the shape index and their average, in relationship to the different samples (HPA, HPB, NPC) and microstructure prediction models (cGAN, DDPM). The analysis indicates that the DDPM provides better results than the cGAN model.

FIB-SEM nano-tomography

The nanotomography experiment is performed by utilizing a Zeiss AURIGA-CrossBeam workstation. The current and voltage are 2 nA and 30 kV and the angle of the FIB to the detector columns is 54° . A layer of platinum is deposited over the sample to decrease charging. The porous copper film is cut into a cubic shape of $20 \times 20 \times 20 \mu\text{m}^3$ by Ga^+ ion milling. The SEM image is taken by a Secondary Electron Secondary Ion (SESI) detector with an acceleration voltage of 30 kV. We mill the cube every 25 nm so that a series of 2D image slices are obtained. We use the line averaging technique with scan speed 8 and $N = 1$ so that noise is reduced. The number of images per sample are 450 images. Overall, we spend 8 h duration per sample.

Image pre-processing

Avizo 3D is used to reconstruct 450 2D images into 3D data. The alignment is performed by FIB stack wizard module with least square method. The

volume of interest (VOI) from each reconstructed 3D dataset is $1120 \times 640 \times 450$ voxel³. The raw 3D data has voxel sizes of 18.6 nm, 18.6 nm, and 25 nm in the x, y, and z directions, respectively. Therefore, each volume is $20.8 \times 11.9 \times 11.3 \mu\text{m}^3$. We cut 3 VOIs of $10 \times 10 \times 10 \mu\text{m}^3$ from this volume for each samples measurements. Each volume contains $538 \times 538 \times 400$ voxels². The curtaining and shadowing artifacts of the obtained tomography image data are reduced with FFT-filter⁶⁹ and histogram shifting methods^{35,38}, respectively. The renderings of images are produced with Avizo 3D.

Relative density and specific surface area formula

We utilize the segmented 3D data, utilizing the U-NET with the hybrid training approach, to evaluate the relative density and specific area. The relative density D is defined as

$$D = \frac{\text{No. of copper voxels}}{\text{Total no. of voxels in VOI}}$$

The specific surface area measurement is done with Avizo 3D software. The surface of the 3D volume is generated with generate_surface module, excluding the surface at the extremities. The software measures the surface area of the pore-copper interface, and the specific surface area SA is calculated with:

$$SA = \frac{\text{pore - copper interface surface area}}{\text{total volume of one VOI}}$$

Skeletonization procedure

We utilize the segmented 3D data, utilizing the U-NET with the hybrid training approach, to perform the skeletonization procedure. Skeletonization is performed by Avizo 3D distance-ordered thinner and distance map modules. The strut diameters are then extracted with the Spatial_Graph_Statistics module. The skeleton's strut diameters are fitted by log-normal distribution with the scipy package in Python. Supplementary Note 4 shows the histogram and the fitted log-normal distribution of HPA, HPB, and NPC.

Curvature measurements

Based on the segmented 3D data, utilizing the U-NET with the hybrid training approach, we perform the curvature analysis. The Avizo 3D curvature module extracts the Gaussian and mean curvature data from the pore-copper surface. The joint probability distribution plot and the mean values of the curvatures are done with the gaussian_kde module and the NumPy package in Python, respectively.

Tortuosity measurements

We utilize the segmented 3D data to evaluate the tortuosity. The geodesic and Euclidian distances are carried out by Python's skfmm library. The two 3D distance arrays are divided with geometric tortuosity τ formula:

$$\tau = \frac{\text{geodesic distance}}{\text{Euclidean distance}}$$

The tortuosity calculation is done with numpy package in Python. Supplementary Fig. 5a–g depicts the 3D tortuosity calculations.

Deep learning annotation and segmentation

We utilize a Fujitsu Celcius M740B workstation. Avizo 3D is applied for the visualization of the segmented volume of interest (VOI). We utilize a U-Net deep learning architecture from Chollet³⁶ in Python as well as apply the open source deep-learning library Keras to segment the pore and copper phases. The developed hybrid model and threshold segmentation (Otsu's algorithm) are used as the training annotations. We use 20% of the data as the training set, i.e., one set of image and annotation set is chosen for

every other five training sets. Within this training set, 70% is set aside as validation set. The optimizer, loss function, batch size, and epochs are rmsprop, sparse categorical crossentropy, 1, and 100, respectively, see Supplementary Note 2. The conventional threshold algorithm (CTA) pore and shine through are combined to get the pore phase. Finally, the segmentation process is finalized by inverting the pore phase.

Multi-variable linear regression model

The evaluated microstructure features extracted from the segmented 3D microstructure data, see Table 2 are used as an input for the MVLR model. We maximize the use of the training set with a leave-one-out cross-validation (LOOCV) to obtain reliable and unbiased results⁵². As a result, 18 conductivity predictions of each unseen validation sample are produced from one LOOCV-set. We average root mean square errors (RMSE) for each model. The model takes the form $\sigma = b_0 + b_1X_1 + \dots + b_nX_n$ where b_0 is a constant, and b_1, \dots, b_n are coefficients of features X_1, \dots, X_n ⁵⁹. The linear regression models are generated and evaluated by Python's sklearn library. First, we standardize the scaling of the data with sklearn's StadarScaler module. Then, we use sklearn's LinearRegression module to find the linear coefficients. RMSE and R^2 are calculated by using mean_squared_error and r2_square modules. We set the number of features to be equal or more than two so that different models with various number of features are calculated. The R^2 values of each material are: $R^2_{\text{HPA}} = 0.97$, $R^2_{\text{HPB}} = 0.61$, $R^2_{\text{NPC}} = 0.99$.

Conditional GAN

We utilize a HP ProLiant DL385 Gen10 workstation with a single A40 GPU. Further, Python's Keras library are used for analysis. The number of images for each temperature class is 1350, so there are 8100 images for the training. The image is resized to 224×224 pixels². The model consists of generator G and discriminator D to generate synthetic data and to distinguish between synthetic and real data, see further details in Supplementary Note 9. G and D are trained together so that G is maximizing misdetection by D ⁷⁰. This framework follows min-max game of two players with the loss function:

$$\min_G \max_D V(D, G) = \mathbb{E}_{x \sim P_{\text{data}}(x)} [\log D(x|y)] + \mathbb{E}_{z \sim p_z(z)} [\log(1 - D(G(z|y)))]$$

where the distribution of real images is P_{data} while z corresponds to the input noise vectors⁷¹.

Denosing diffusion probabilistic model

The model is implemented using the PyTorch library on a single HP ProLiant A40 GPU Gen10 server. Similar to cGAN, each temperature class contains 1350 images, and the image is resized to 224×224 pixels². In total, there are 8100 images for the training. The forward diffusion process $q(x_t|x_{t-1})$ gradually adds Gaussian noise to the initial image x_0 . The probability density function of the noisier image x_t from the previous less noisy image x_{t-1} is

$$q(x_t|x_{t-1}) := N(x_t; \sqrt{1 - \beta_t}x_{t-1}, \beta_t I)$$

with linear variance schedule β_1, \dots, β_t where t is the time step and I is the identity matrix¹⁰.

Using notation $\alpha_t := 1 - \beta_t$ and $\bar{\alpha}_t := \prod_{s=1}^t \alpha_s$. The noisy image at an arbitrary time step t is

$$q(x_t|x_0) = N(x_t; \sqrt{\bar{\alpha}_t}x_0, (1 - \bar{\alpha}_t)I)$$

With re-parametrization, image at arbitrary time t can be obtained directly with

$$x_t = \sqrt{\bar{\alpha}_t}x_0 + \sqrt{1 - \bar{\alpha}_t}\epsilon$$

where, $\epsilon \sim N(\epsilon|0, I)$

The reverse diffusion process $p(x_{t-1}|x_t)$ aims to denoise the image iteratively to a less noisy image and it is defined:

$$p(x_{t-1}|x_t) := N(x_{t-1}; \tilde{\mu}_t(x_t, t), \sigma_t^2 I)$$

Because the variance σ_t^2 is fixed to a certain schedule. The mean of noise is estimated with

$$\tilde{\mu}_t(x_t, t) \approx \frac{1}{\sqrt{\alpha_t}} \left(x_t - \frac{1 - \alpha_t}{\sqrt{1 - \alpha_t}} \epsilon_t \right)$$

where ϵ_t is the noise introduced in step t . We can train neural network $\epsilon_\theta(x_t, t)$ (see Supplementary Note 10) to approximate ϵ_t minimizing

$$L_\theta = \|\epsilon_t - \epsilon_\theta(x_t, t)\|^2$$

Slice 2D shape index

Based on the segmented image data utilizing the U-NET with the hybrid training we perform the curvature analysis. The shape index used for the analysis of the real and synthetically reconstructed image relates to the local curvature measurement. Its value lies between -1 and 1, where 1 represents 'spherical caps'⁷². The analysis is performed by utilizing the shape_index module in the python's scikit-image library.

Data availability

All data that support the findings of this study are available from the corresponding author upon reasonable request.

Code availability

All code that support the findings of this study are available from the corresponding author upon reasonable request.

Received: 8 August 2023; Accepted: 4 April 2024;

Published online: 24 April 2024

References

- Ramprasad, R., Batra, R., Pilia, G., Mannodi-Kanakkithodi, A. & Kim, C. Machine learning in materials informatics: Recent applications and prospects. *npj Comput. Mater.* **3**, 54 (2017).
- Navarro, P. J., Fernández, C., Borraz, R. & Alonso, D. A machine learning approach to pedestrian detection for autonomous vehicles using high-definition 3D range data. *Sensors* **17**, 18 (2017).
- Harrison, C. J. & Sidey-Gibbons, C. J. Machine learning in medicine: a practical introduction to natural language processing. *BMC Med. Res. Methodol.* **21**, 1–11 (2021).
- Wang, Y. et al. All-weather, natural silent speech recognition via machine-learning-assisted tattoo-like electronics. *npj Flex. Electron.* **5**, 1–9 (2021).
- Zhou, T., Song, Z. & Sundmacher, K. Big Data Creates New Opportunities for Materials Research: A Review on Methods and Applications of Machine Learning for Materials Design. *Engineering* **5**, 1017–1026 (2019).
- Jablonka, K. M., Ongari, D., Moosavi, S. M. & Smit, B. Big-Data Science in Porous Materials: Materials Genomics and Machine Learning. *Chem. Rev.* **120**, 8066–8129 (2020).
- Kondo, R., Yamakawa, S., Masuoka, Y., Tajima, S. & Asahi, R. Microstructure recognition using convolutional neural networks for prediction of ionic conductivity in ceramics. *Acta Mater.* **141**, 29–38 (2017).
- Guo, P., Meng, W., Xu, M., Li, V. C. & Bao, Y. Predicting mechanical properties of high-performance fiber-reinforced cementitious composites by integrating micromechanics and machine learning. *Materials* **14**, 3143 (2021).
- Shiraiwa, T., Miyazawa, Y. & Enoki, M. Prediction of fatigue strength in steels by linear regression and neural network. *Mater. Trans.* **60**, 189–198 (2019).
- Ho, J., Jain, A. & Abbeel, P. Denoising diffusion probabilistic models. *Adv. Neural Inf. Process. Syst.* **2020**, 1–25 (2020).
- Sanchez-Lengeling, B. & Aspuru-Guzik, A. Inverse molecular design using machine learning: Generative models for matter engineering. *Science* **361**, 360–365 (2018).
- Kim, B., Lee, S. & Kim, J. Inverse design of porous materials using artificial neural networks. *Sci. Adv.* **6**, 1–8 (2020).
- Albahli, S. Efficient gan-based chest radiographs (CXR) augmentation to diagnose coronavirus disease pneumonia. *Int. J. Med. Sci.* **17**, 1439–1448 (2020).
- Tang, J. et al. Machine learning-based microstructure prediction during laser sintering of alumina. *Sci. Rep.* **11**, 1–10 (2021).
- Chun, S. et al. Deep learning for synthetic microstructure generation in a materials-by-design framework for heterogeneous energetic materials. *Sci. Rep.* **10**, 1–15 (2020).
- Amiri, H., Vasconcelos, I., Jiao, Y., Chen, P. E. & Plümper, O. Quantifying microstructures of earth materials using higher-order spatial correlations and deep generative adversarial networks. *Sci. Rep.* **13**, 1–19 (2023).
- Thanh-Tung, H. & Tran, T. On Catastrophic Forgetting and Mode Collapse in Generative Adversarial Networks. *arXiv* <https://arxiv.org/abs/1807.04015> (2018).
- Lee, K. H. & Yun, G. J. Microstructure reconstruction using diffusion-based generative models. *Mech. Adv. Mater. Struct.* <https://doi.org/10.1080/15376494.2023.2198528> (2023).
- Iassonov, P., Gebrenegus, T. & Tuller, M. Segmentation of X-ray computed tomography images of porous materials: A crucial step for characterization and quantitative analysis of pore structures. *Water Resour. Res.* **45**, W09415 (2009).
- Richert, C., Wu, Y., Hablitzel, M., Lilleodden, E. T. & Huber, N. Image segmentation and analysis for densification mapping of nanoporous gold after nanoindentation. *MRS Adv.* **6**, 519–523 (2021).
- Joos, J., Carraro, T., Weber, A. & Ivers-Tiffée, E. Reconstruction of porous electrodes by FIB/SEM for detailed microstructure modeling. *J. Power Sources* **196**, 7302–7307 (2011).
- Čalkovský, M. et al. Comparison of segmentation algorithms for FIB-SEM tomography of porous polymers: Importance of image contrast for machine learning segmentation. *Mater. Charact.* **171**, 110806 (2021).
- Roberge, H., Moreau, P., Couallier, E. & Abellan, P. Determination of Selective Layer Thickness and Permeability of PAN and PES Polymeric Filtration Membranes Using 3D FIB/SEM. *SSRN Electron. J.* **653**, 120530 (2022).
- Wijaya, A. et al. Development of a Characterization Workflow for Reliable Porous Copper Films SEM-FIB Tomography and Advanced Image Analysis. *Proc. ISTFA 277–282*, <https://doi.org/10.31399/asm.cp.istfa2019p0277> (2019).
- Durmaz, A. R. et al. A deep learning approach for complex microstructure inference. *Nat. Commun.* **12**, 1–15 (2021).
- Müller, S. et al. Deep learning-based segmentation of lithium-ion battery microstructures enhanced by artificially generated electrodes. *Nat. Commun.* **12**, 1–12 (2021).
- Minaee, S. et al. Image Segmentation Using Deep Learning: A Survey. *IEEE Trans. Pattern Anal. Mach. Intell.* 1–22, <https://doi.org/10.1109/TPAMI.2021.3059968> (2021).
- Ronneberger, O., Fischer, P. & Brox, T. U-Net: Convolutional Networks for Biomedical Image Segmentation. *Med. Image Comput. Comput. Interv.* **9351**, 234–241 (2015).
- Vorauer, T. et al. Impact of solid-electrolyte interphase reformation on capacity loss in silicon-based lithium-ion batteries. *Commun. Mater.* **4**, 1–12 (2023).

30. Chang, J. et al. Deep learning segmentation of hyperautofluorescent fleck lesions in Stargardt disease. *Sci. Rep.* **10**, 1–13 (2020).
31. Atici, U. Prediction of the strength of mineral admixture concrete using multivariable regression analysis and an artificial neural network. *Expert Syst. Appl.* **38**, 9609–9618 (2011).
32. Kwak, S. et al. Using multiple regression analysis to predict directionally solidified TiAl mechanical property. *J. Mater. Sci. Technol.* **104**, 285–291 (2022).
33. Sinojiya, R. J. et al. Probing the composition dependence of residual stress distribution in tungsten-titanium nanocrystalline thin films. *Commun. Mater.* **4**, 11 (2023).
34. Kronberg, R., Lappalainen, H. & Laasonen, K. Hydrogen Adsorption on Defective Nitrogen-Doped Carbon Nanotubes Explained via Machine Learning Augmented DFT Calculations and Game-Theoretic Feature Attributions. *J. Phys. Chem. C.* **125**, 15918–15933 (2021).
35. Wijaya, A. et al. Multi-method characterization approach to facilitate a strategy to design mechanical and electrical properties of sintered copper. *Mater. Des.* **197**, 109188 (2021).
36. Chollet, F. Image segmentation with a U-Net-like architecture. https://keras.io/examples/vision/oxford_pets_image_segmentation/ (2019).
37. Su, Z. et al. Artificial neural network approach for multiphase segmentation of battery electrode nano-CT images. *npj Comput. Mater.* **8**, 30 (2022).
38. Taillon, J. A., Pellegrinelli, C., Huang, Y. L., Wachsmann, E. D. & Salamanca-Riba, L. G. Improving microstructural quantification in FIB/SEM nanotomography. *Ultramicroscopy* **184**, 24–38 (2018).
39. Otsu, N. A Threshold Selection Method from Gray-Level Histograms. *IEEE Trans. Syst. Man. Cybern.* **9**, 62–66 (1979).
40. Achanta, R. et al. SLIC superpixels compared to state-of-the-art superpixel methods. *IEEE Trans. Pattern Anal. Mach. Intell.* **34**, 2274–2281 (2012).
41. Taha, A. A. & Hanbury, A. Metrics for evaluating 3D medical image segmentation: Analysis, selection, and tool. *BMC Med. Imaging* **15**, 1–28 (2015).
42. Kazak, A., Simonov, K. & Kulikov, V. Machine-Learning-Assisted Segmentation of Focused Ion Beam-Scanning Electron Microscopy Images with Artifacts for Improved Void-Space Characterization of Tight Reservoir Rocks. *SPE J.* **26**, 1739–1758 (2021).
43. Wang, D., Wang, X., Xu, C., Fu, Z. & Zhang, J. Densification mechanism of the ultra-fast sintering dense alumina. *AIP Adv.* **10**, 025223 (2020).
44. Kang, S.-J. L. *Sintering Densification, Grain Growth and Microstructure*. (Butterworth-Heinemann, 2005).
45. German, R. M. Sintering Trajectories: Description on How Density, Surface Area, and Grain Size Change. *JOM* **68**, 878–884 (2016).
46. Peyregab, C. & Jeulin, D. Estimation of tortuosity and reconstruction of geodesic paths in 3D. *Image Anal. Stereol.* **32**, 27–43 (2013).
47. Tolnai, D. et al. In situ synchrotron tomographic investigation of the solidification of an AlMg_{4.7}Si₈ alloy. *Acta Mater.* **60**, 2568–2577 (2012).
48. Dopazo, C., Martín, J. & Hierro, J. Local geometry of isoscalar surfaces. *Phys. Rev. E Stat. Nonlinear Soft Matter Phys.* **76**, 1–11 (2007).
49. Avramović, L. et al. Influence of the shape of copper powder particles on the crystal structure and some decisive characteristics of the metal powders. *Metals (Basel)*. **9**, 56 (2019).
50. German, R. Geometric Trajectories during Sintering. In *Sintering: From Empirical Observations to Scientific Principles* 141–181, <https://doi.org/10.1016/C2012-0-00717-X> (2014).
51. Schneider, A., Hommel, G. & Blettner, M. Linear Regression Analysis - Part 14 of a Series on Evaluation of Scientific Publications. *Dtsch. Arztebl.* **107**, 776–782 (2010).
52. Agrawal, A. et al. Exploration of data science techniques to predict fatigue strength of steel from composition and processing parameters. *Integr. Mater. Manuf. Innov.* **3**, 90–108 (2014).
53. Ebner, M., Chung, D. W., García, R. E. & Wood, V. Tortuosity anisotropy in lithium-ion battery electrodes. *Adv. Energy Mater.* **4**, 1–6 (2014).
54. Iyer, A., Dey, B., Dasgupta, A., Chen, W. & Chakraborty, A. A Conditional Generative Model for Predicting Material Microstructures from Processing Methods. NeurIPS 2019 Vancouver, Canada (2019).
55. Matsuda, Y., Ookawara, S., Yasuda, T., Yoshikawa, S. & Matsumoto, H. Framework for discovering porous materials: Structural hybridization and Bayesian optimization of conditional generative adversarial network. *Digit. Chem. Eng.* **5**, 100058 (2022).
56. Azqadan, E., Jahed, H. & Arami, A. Predictive microstructure image generation using denoising diffusion probabilistic models. *Acta Mater.* **261**, 119406 (2023).
57. Bostanabad, R. et al. Computational microstructure characterization and reconstruction: Review of the state-of-the-art techniques. *Prog. Mater. Sci.* **95**, 1–41 (2018).
58. Ternero, F., Rosa, L. G., Urban, P., Montes, J. M. & Cuevas, F. G. Influence of the total porosity on the properties of sintered materials—a review. *Metals*. **11**, 730 (2021).
59. Darlington, R. B. & Hayes, A. F. *Regression Analysis and Linear Models Concepts, Applications, and Implementation* (The Guilford Press, 2016).
60. Nguyen, P. C. H. et al. Synthesizing controlled microstructures of porous media using generative adversarial networks and reinforcement learning. *Sci. Rep.* **12**, 1–16 (2022).
61. Hsu, T. et al. Microstructure Generation via Generative Adversarial Network for Heterogeneous, Topologically Complex 3D Materials. *JOM* **73**, 90–102 (2021).
62. Shimada, H. et al. Nanocomposite electrodes for high current density over 3 A cm⁻² in solid oxide electrolysis cells. *Nat. Commun.* **10**, 1–10 (2019).
63. Pretschuh, P., Egger, A., Brunner, R. & Bucher, E. Electrochemical and microstructural characterization of the high-entropy perovskite La_{0.2}Pr_{0.2}Nd_{0.2}Sm_{0.2}Sr_{0.2}CoO_{3-δ} for solid oxide cell air electrodes. *Fuel Cells*, <https://doi.org/10.1002/fuce.202300036> (2023).
64. Liu, Y. et al. Development of the cold sintering process and its application in solid-state lithium batteries. *J. Power Sources* **393**, 193–203 (2018).
65. Guo, X., Xun, Q., Li, Z. & Du, S. Silicon carbide converters and MEMS devices for high-temperature power electronics: A critical review. *Micromachines* **10**, 406 (2019).
66. Vorauer, T. et al. Multi-scale quantification and modeling of aged nanostructured silicon-based composite anodes. *Commun. Chem.* **3**, 1–11 (2020).
67. Padurariu, L. et al. Analysis of local vs. macroscopic properties of porous BaTiO₃ ceramics based on 3D reconstructed ceramic microstructures. *Acta Mater.* **255**, 119084 (2023).
68. Allendorf, M. D. et al. Challenges to developing materials for the transport and storage of hydrogen. *Nat. Chem.* **14**, 1214–1223 (2022).
69. Liu, Y., King, H. E., van Huis, M. A., Drury, M. R. & Plümpner, O. Nanotomography of porous geological materials using focused ion beam-scanning electron microscopy. *Minerals* **6**, 104 (2016).
70. Goodfellow, I. J. et al. Generative Adversarial Networks. *Adv. Neural Inf. Process. Syst.* **2017**, 4089–4099 (2014).
71. Mirza, M. & Osindero, S. Conditional Generative Adversarial Nets. arXiv preprint, [arXiv: 1411.1784](https://arxiv.org/abs/1411.1784) (2014).
72. Koenderink, J. J. & van Doorn, A. J. Surface shape and curvature scales. *Image Vis. Comput.* **10**, 557–564 (1992).

Acknowledgements

We acknowledge the financial support by Die Österreichische Forschungsgesellschaft (FFG) under NanoPore, Proj. No. 883905. and partly under ProQualiCu, Proj. No. 853467. We thank B. Eichinger for the preparation of the samples. The authors gratefully acknowledge the financial support under the scope of the COMET program within the K2 Center

“Integrated Computational Material, Process and Product Engineering (IC-MPPE)” (Project No 886385). This program is supported by the Austrian Federal Ministries for Climate Action, Environment, Energy, Mobility, Innovation and Technology (BMK) and for Labour and Economy (BMAW), represented by the Austrian Research Promotion Agency (FFG), and the federal states of Styria, Upper Austria and Tyrol, P. No. P2.22 ECOSolder.

Author contributions

R.B. planned and A.W. performed the image analysis work. A.W. developed the image analysis workflows and accelerated material platform under supervision of R.B. R.B., J.W. A.W. and B.S. planned and conducted the FIB-SEM measurements. R.B. and A.W. wrote the paper. All authors discussed the results and commented on the paper. R.B. planned the whole project.

Competing interests

The authors declare no competing interests.

Additional information

Supplementary information The online version contains supplementary material available at <https://doi.org/10.1038/s43246-024-00493-5>.

Correspondence and requests for materials should be addressed to Roland Brunner.

Peer review information *Communications Materials* thanks the anonymous reviewers for their contribution to the peer review of this work. Primary Handling Editors: Jet-Sing Lee. A peer review file is available.

Reprints and permissions information is available at <http://www.nature.com/reprints>

Publisher's note Springer Nature remains neutral with regard to jurisdictional claims in published maps and institutional affiliations.

Open Access This article is licensed under a Creative Commons Attribution 4.0 International License, which permits use, sharing, adaptation, distribution and reproduction in any medium or format, as long as you give appropriate credit to the original author(s) and the source, provide a link to the Creative Commons licence, and indicate if changes were made. The images or other third party material in this article are included in the article's Creative Commons licence, unless indicated otherwise in a credit line to the material. If material is not included in the article's Creative Commons licence and your intended use is not permitted by statutory regulation or exceeds the permitted use, you will need to obtain permission directly from the copyright holder. To view a copy of this licence, visit <http://creativecommons.org/licenses/by/4.0/>.

© The Author(s) 2024